An Operando Investigation of (Ni–Fe–Co–Ce)O_x System as Highly Efficient Electrocatalyst for Oxygen Evolution Reaction

Marco Favaro,[†,‡,§,¶] Walter S. Drisdell,[‡,§,¶] Matthew A. Marcus,[†] John M. Gregoire,[∥] Ethan J. Crumlin,[*,†] Joel A. Haber,[*,∥] and Junko Yano[*,‡,§,⊥]

[†]Advanced Light Source, Lawrence Berkeley National Laboratory, One Cyclotron Road, Berkeley, California 94720, United States

[‡]Joint Center for Artificial Photosynthesis, Lawrence Berkeley National Laboratory, One Cyclotron Road, Berkeley, California 94720, United States

[§]Chemical Sciences Division, Lawrence Berkeley National Laboratory, One Cyclotron Road, Berkeley, California 94720, United States

[∥]Joint Center for Artificial Photosynthesis, California Institute of Technology, Pasadena, California 91125, United States

[⊥]Molecular Biophysics and Integrated Bioimaging Division, Lawrence Berkeley National Laboratory, One Cyclotron Road, Berkeley, California 94720, United States

Supporting Information

ABSTRACT: The oxygen evolution reaction (OER) is a critical component of industrial processes such as electrowinning of metals and the chlor-alkali process. It also plays a central role in the development of a renewable energy field for generation a solar fuels by providing both the protons and electrons needed to generate fuels such as H_2 or reduced hydrocarbons from CO_2. To improve these processes, it is necessary to expand the fundamental understanding of catalytically active species at low overpotential, which will further the development of electrocatalysts with high activity and durability. In this context, performing experimental investigations of the electrocatalysts under realistic working regimes (i.e., under operando conditions) is of crucial importance. Here, we study a highly active quinary transition-metal-oxide-based OER electrocatalyst by means of operando ambient-pressure X-ray photoelectron spectroscopy and X-ray absorption spectroscopy performed at the solid/liquid interface. We observe that the catalyst undergoes a clear chemical-structural evolution as a function of the applied potential with Ni, Fe, and Co oxyhydroxides comprising the active catalytic species. While CeO_2 is redox inactive under catalytic conditions, its influence on the redox processes of the transition metals boosts the catalytic activity at low overpotentials, introducing an important design principle for the optimization of electrocatalysts and tailoring of high-performance materials.

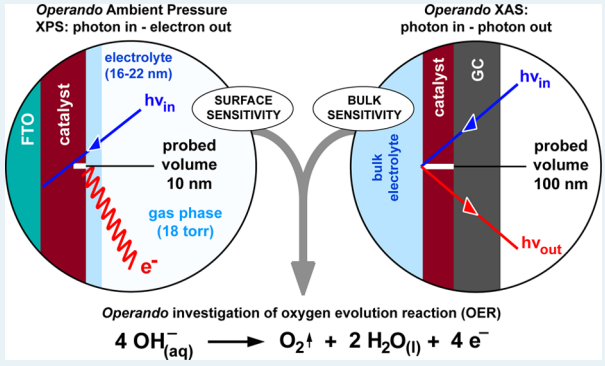

KEYWORDS: *oxygen evolution reaction (OER), transiton metal oxides, operando techniques, ambient pressure, catalytic conditions, synchrotron radiation, electron spectroscopies*

INTRODUCTION

Discovering improved electrocatalysts for the oxygen evolution reaction (OER) is of great importance for sustainable energy conversion.[1−3] Ascertaining structure−property relationships remains a central challenge in the field of heterogeneous catalysis and comprises an important strategy for the development of superior electrocatalysts.[4−6] Enhanced catalytic activity has been ascribed to amorphous materials as heterogeneous catalysts and OER electrocatalysts,[7−18] while high activity and stability has also been reported for nanostructured, multiphase heterogeneous catalysts and electrocatalysts, with the behavior attributed to cooperative effects like spillover or unique interfacial crystallographic structures.[19−21] Among the most active and investigated OER electrocatalysts in basic electrolytes are transition-metal oxyhydroxides.[22−27] Their high activity is ascribed in part to volume activity of the hydrated catalyst. However, the role of adventitious iron contamination[28−31] and their behavior as "adaptive junctions"[32,33] (i.e., the change in structure, oxidation, hydration, etc. when placed under operating potential) has confounded identification of activity trends of the transition metals and catalytically active metal centers.[34−36]

We recently reported a high-throughput investigation of the (Ni−Fe−Co−Ce)O_x composition space which identified a new, unpredicted Ce-rich composition region of active OER electrocatalysts.[37] Given the comparatively low activity of

Received: November 2, 2016
Revised: December 19, 2016
Published: December 27, 2016

CeO_x, the high catalytic activity of the Ce-rich catalyst is quite surprising, motivating detailed study of this catalyst. Previous ex situ structural characterization of the $Ni_{0.3}Fe_{0.07}Co_{0.2}Ce_{0.43}O_x$ catalyst using both XAS and low-dose, high-resolution TEM demonstrated that the catalyst is a two-phase nanocomposite in which CeO_2 nanoparticles form atomically sharp grain boundaries with alloyed transition-metal oxides.[38] While examination of the as-synthesized and postoperation catalyst revealed no significant changes to the structure or chemistry,[38] understanding the catalytic activity enabled by the nanostructure requires detailed characterization under polarization (i.e., as a function of the applied potential), which is reported herein.

In pH 14 electrolyte, $Ni_{0.3}Fe_{0.07}Co_{0.2}Ce_{0.43}O_x$ exhibits comparable performance to optimal mixed-transition metal oxides at moderate overpotential and current density, in particular, near 10 mA cm^{-2}. At lower current density and overpotential, $Ni_{0.3}Fe_{0.07}Co_{0.2}Ce_{0.43}O_x$ outperforms all other catalysts in the $(Ni-Fe-Co-Ce)O_x$ composition space. This behavior can be represented in terms of the effective Tafel parameters, with the Ce-rich catalyst exhibiting twice the effective Tafel slope and orders of magnitude larger effective exchange current density than that of the previously reported $(Ni-Fe)O_x$ and $(Ni-Co)O_x$ catalysts.[37,39] The effective Tafel behavior was found to correlate with the average redox potential in the mixed-metal oxide catalyst, which we further explore in the present work to elucidate the role of Ce in the quinary oxide catalyst.

Ce is well-known as an oxygen reservoir in oxidation reactions because of its low redox potential and is known to be a good oxygen-ion conductor with high surface-oxygen exchange density at elevated temperatures.[40−45] Oxygen conductivity, surface-oxygen mobility and oxygen donation to cocatalysts are enhanced in nanostructured CeO_2 and are mediated by grain boundaries and segregation of other cations therein.[43,44] Recent work has capitalized on these unique properties of nanocrystalline CeO_2 for enhancing the activity of Pd- and Pt-based electrocatalysts for the oxygen reduction reaction (ORR), and detailed calculations have revealed the importance of oxygen spillover from ceria nanoparticles onto Pt.[46−52]

The spillover of oxygen from CeO_2 to the transition metal oxides in $Ni_{0.3}Fe_{0.07}Co_{0.2}Ce_{0.43}O_x$ could alter the transition metal species under operational conditions, motivating the examination of this catalyst with a suite of advanced in situ and operando X-ray spectroscopies. These recently developed synchrotron techniques enable characterization of the potential-dependent oxidation states and chemical structures of electrocatalysts under realistic operating conditions. The methods have provided element-specific characterization of catalysts[53,54] and illustrated the importance of collecting data under functional conditions.[55−60] In the present work, we advance the state-of-the-art of these techniques with the interrogation of the quinary oxide catalyst. We investigate the role of each transition-metal−Ce oxide using two operando techniques (defined here as actively performing OER under potentiostatic control): ambient pressure X-ray photoelectron spectroscopy (APXPS) as a surface probe and X-ray absorption spectroscopy (XAS) as a bulk-probe. Combined information from these two techniques provides detailed insights of the location and the role of each metal oxide during OER electrocatalysis.

RESULTS AND DISCUSSION

To identify the operating potentials of interest for operando characterization of the active electrocatalytic species, we first conduct a combinatorial investigation[37,39] of the redox behavior in the $(Ni-Fe-Co-Ce)O_x$ system by acquiring cyclic voltammograms (CVs, aqueous 1 M NaOH electrolyte) for a series of catalyst compositions.[37,39] The electrochemical current in each CV has contributions from capacitive charging, redox reactions of the electrocatalyst, and electrocatalysis, the last of which is relatively insensitive to the potential scan rate. To increase the relative signal from the redox reactions, we perform CVs at 0.25 V s^{-1} and sacrifice the observation of the onset of electrocatalytic activity, which was the focus of previous work.[37] Given the ex situ segregation of CeO_2 from the transition-metal oxides, the behavior of $Ni_{0.3}Fe_{0.07}Co_{0.2}Ce_{0.43}O_x$ with respect to Ni−Fe and Ni−Co oxides is of particular interest, especially due to the previous reports on the active species in Ni−Fe and Co-based OER catalysts (see below). Figure 1 shows CVs for 18 metal oxide compositions that lie along three composition lines illustrated in Figure 1a.

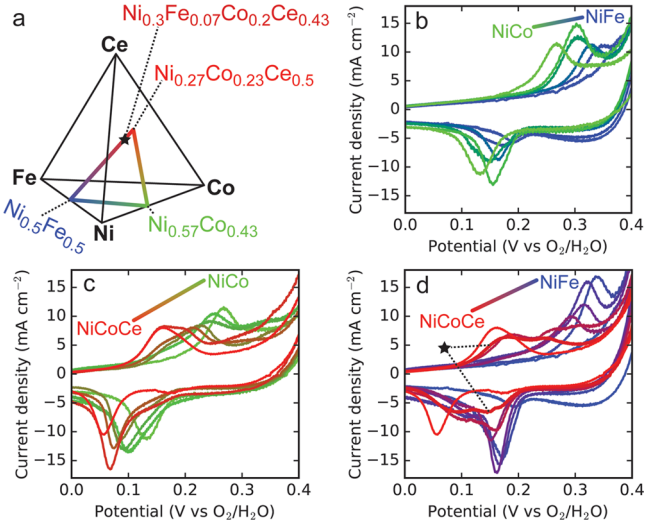

Figure 1. Color-coded composition lines in the Ni−Fe−Co−Ce oxide space (a) are shown with labeled end-point compositions. The catalyst redox regions of CVs acquired at 0.25 V s^{-1} are shown (b−d) for a series of compositions along each of the composition lines, with the $Ni_{0.3}Fe_{0.07}Co_{0.2}Ce_{0.43}O_x$ catalyst noted by a star in panels a and d. The high current density from the noncatalytic processes obscure the onset of OER electrocatalysis. The composition of each catalyst is provided in Table S1.

Starting from $Ni_{0.5}Fe_{0.5}O_x$ and extending to $Ni_{0.57}Co_{0.43}O_x$, Figure 1b shows that the catalyst redox processes systematically shift to lower potential; this shift is due in part to the removal of Fe, which has been shown to increase the redox potential of $Ni^{(II/III)}$. Figure 1c shows that the addition of Ce to Ni−Co results in a further decrease in redox potentials, thereby indicating a substantial influence of Ce on the redox processes of Ni and/or Co. Figure 1d covers the range of quinary oxide catalysts between the Ni−Fe and Ni−Co−Ce end-members in Figure 1b,c, which includes the $Ni_{0.3}Fe_{0.07}Co_{0.2}Ce_{0.43}O_x$ catalyst, further illustrating that the addition of Ce to these transition-metal oxides results in systematic lowering of redox potentials. For the quinary oxide catalysts in this series of CVs, there is a broad range of potentials over which redox activity is observed, likely due to overlapping signals from a variety of redox

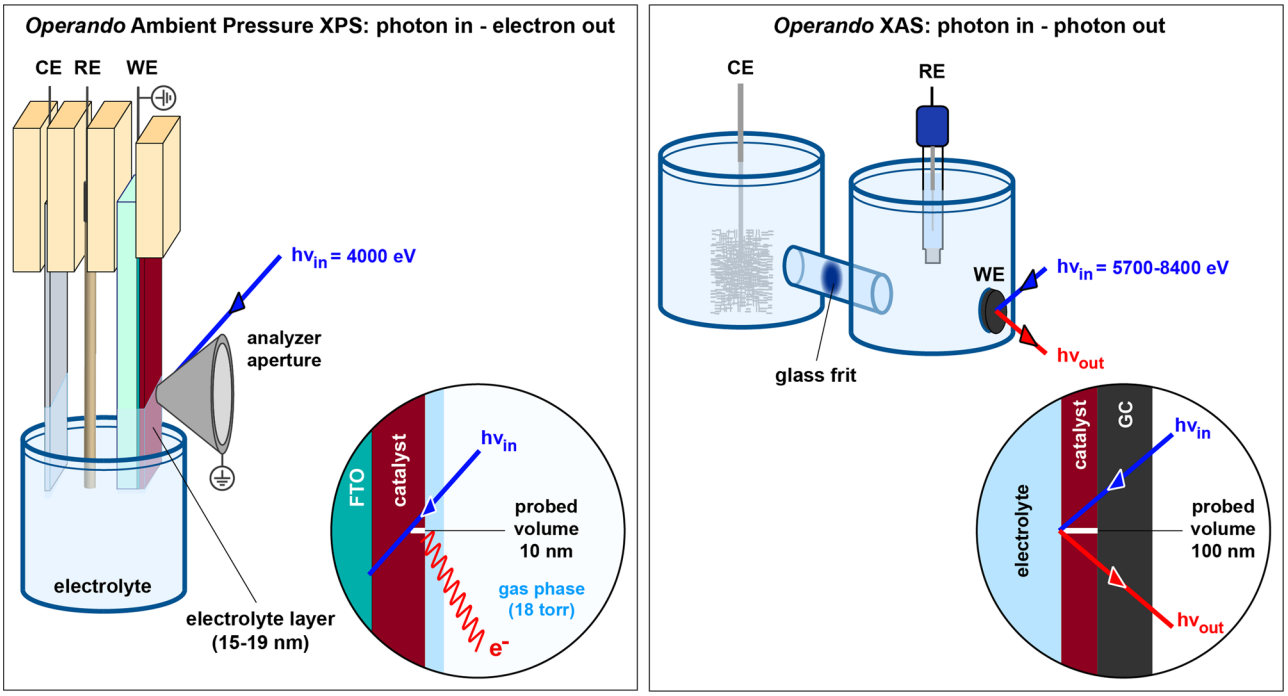

Figure 2. Schematic representation the APXPS and XAS setups, used in this work for the operando characterization of the quinary metal oxide OER electrocatalyst. The insets show the different detection mode of the two techniques and the corresponding probed volume.

processes. In particular, inspection of the anodic sweep of the $Ni_{0.3}Fe_{0.07}Co_{0.2}Ce_{0.43}O_x$ CV reveals multiple oxidation processes that span a 0.2 V interval with redox onset at approximately 0.2 V lower potential than the Ni−Fe sample ($Ni_{0.5}Fe_{0.5}O_x$) and 0.1 V lower potential than the Ni−Co sample ($Ni_{0.57}Co_{0.43}O_x$). These results, combined with the recently documented spillover effect of nanocrystalline CeO_2 in ORR catalysts, bring into question the chemical nature of the Ni, Fe, and Co in the active catalyst in the OER overpotential range of 0.3−0.4 V, in particular, whether the addition of Ce results in the introduction of new (hydro)oxide species that give rise to its superior electrocatalytic performance at low overpotential and current density.

To directly probe the catalyst chemistry under these conditions, the $Ni_{0.3}Fe_{0.07}Co_{0.2}Ce_{0.43}O_x$ catalyst was studied under operando electrochemical conditions by means of "tender" X-ray (2−5 keV) APXPS[61,62] and hard X-ray (in the 5−9 keV range) XAS (using the fluorescence yield detection mode). The two techniques detect photoelectrons and fluoresced photons, respectively, leading to a different probed volume within the catalyst under operating conditions, as schematically reported in Figure 2. In the case of photoelectron detection, the probed volume is confined to the first 10 nm of the materials surface, with the sampling depth depending upon the kinetic energy of the incoming photons. The advantage of using "tender" X-rays for the APXPS measurement is that the effective attenuation lengths (EAL) of the photoelectrons are much larger than with soft X-rays, enabling the study of sample surfaces buried by a nanometric-thick electrolyte layer,[63] as schematically shown in Figure 2. On the other hand, using a photon in−photon out method with excitation energies within the hard X-ray regime enables the study of materials with a probe depth of several microns. Synergistic coupling of the two techniques yields complementary information about the surface chemistry (XPS) and the coordination shell structure of the elements distributed throughout the material (XAS).

It is also important to note the different electrochemical conditions investigated with operando APXPS and XAS. The physical arrangement of the APXPS experiment necessitates the use of lower current densities,[64] which is well-suited for the study of $Ni_{0.3}Fe_{0.07}Co_{0.2}Ce_{0.43}O_x$ at low OER overpotential. For the operando XAS measurements, the sample is immersed in bulk electrolyte, enabling higher diffusion rates and electrocatalytic current densities, which is well-suited for the study of $Ni_{0.3}Fe_{0.07}Co_{0.2}Ce_{0.43}O_x$ at an OER overpotential where its activity is comparable to that of Ni−Fe oxides. The combination of these techniques is a powerful approach for understanding the active catalyst species and the role of Ce in enhancing the activity at low overpotential.

XPS has long been valuable for studying the surfaces of solids in vacuum by providing critical information regarding the composition and chemistry near the sample surface.[65] Recent advances have extended the operational window of this technique from high vacuum conditions to higher pressures, enabling the examination of surfaces under operational and near-operational conditions.[63] In this work, the surface of the electrocatalyst was studied after creating an electrolyte liquid layer, having a thickness between 15 and 19 nm, by the "dip and pull method"[63] and characterized in the anodic regime up to and including the OER condition (hereafter labeled as "catalytic conditions"). The cyclic voltammetry and the corresponding chronoamperometry measurements are reported in Figure S1a−c. Previous studies[61,62] found that addition of 0.1 M KF to the 1.0 M KOH solution facilitated formation and stability of a stable solid/liquid interface. Because oxygen evolution in alkaline conditions consumes hydroxyls, the potential applied to the WE affects the stability of the nanometers-thick electrolyte layer. Keeping this potential constant, it has been found that adding 50−100 mM of a supporting electrolyte enhances the stability of the solid/liquid interface. Comparison between Figure S1a,b indicates that the presence of KF does not appreciably influence the catalytic

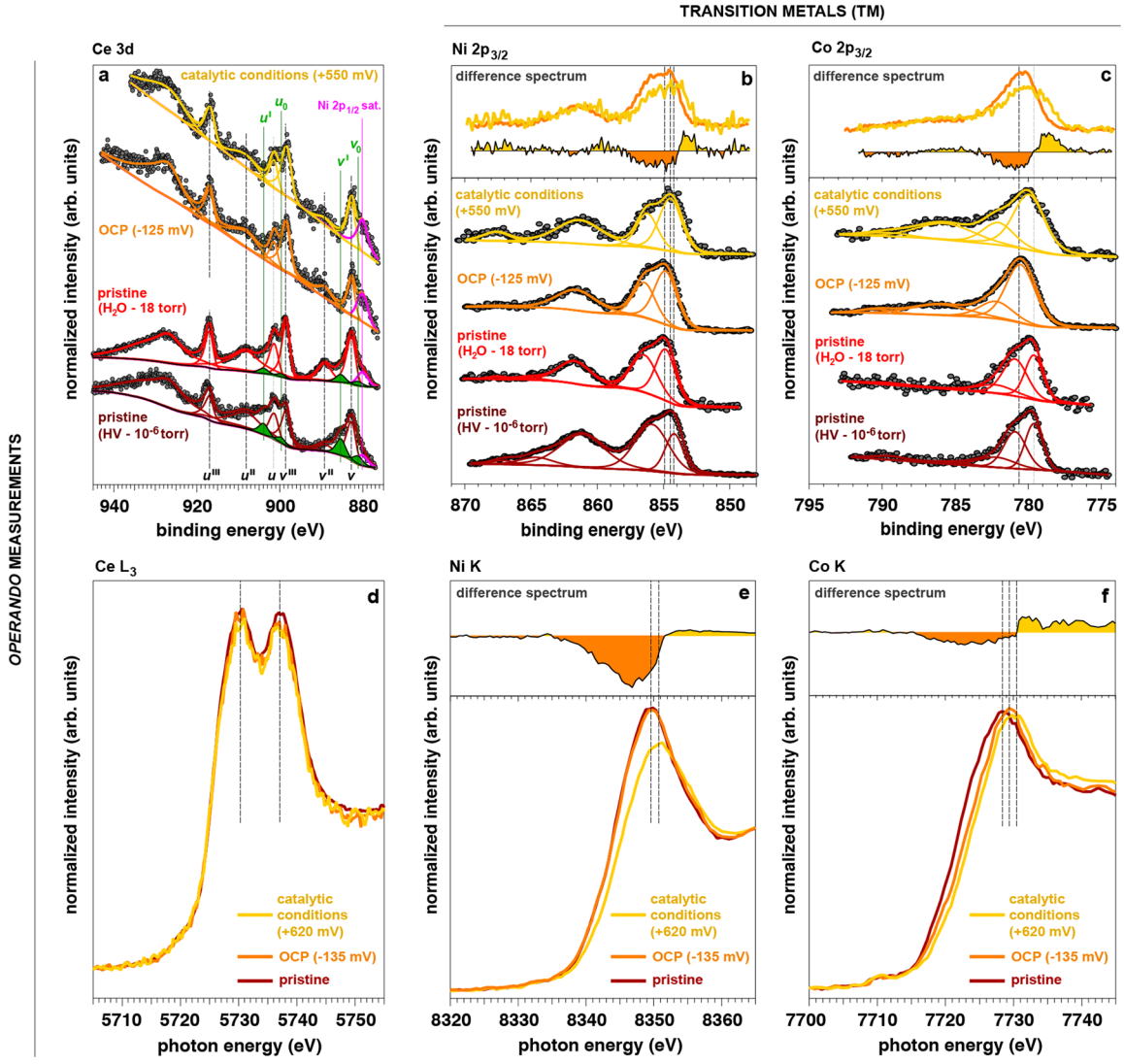

Figure 3. Top: operando APXPS at the Ce 3d (a), Ni $2p_{3/2}$ (b), and Co $2p_{3/2}$ (c) photoelectron peaks acquired under different conditions (see text). To highlight the chemical changes in Ni and Co, the top part of (b) and (c) reports the difference spectrum obtained by subtracting the normalized peak acquired at the OCP from the normalized peak corresponding to the catalytic conditions. Bottom: operando XAS for the pristine quinary metal oxide catalyst, at the OCP and under catalytic conditions, at the Ce L_3 (d) and at the Ni (e) and Co (f) edges. The potentials are with respect to the $Ag/AgCl/Cl^-_{(sat.)}$ reference electrode.

behavior of the quinary metal oxide catalyst, although higher current densities for the redox waves are observed. At these lower scan rates, the redox waves appear more symmetric than those observed in Figure 1d and are observed at comparable potentials. The OER operando condition for the APXPS was chosen to be 0.55 V versus Ag/AgCl, which corresponds to an OER overpotential of approximately 0.34 V and a current density slightly below 1 mA cm^{-2}. At this overpotential, the $Ni_{0.3}Fe_{0.07}Co_{0.2}Ce_{0.43}O_x$ was previously observed[37] to exhibit 1.4 and 7.7 mA cm^{-2} in scanning droplet cell and rotating disc electrode experiments (in 1 M NaOH), respectively, indicating agreement in catalytic performance up to the variations in the mass transport properties of the cells. This potential exceeds that of the redox processes of $Ni_{0.3}Fe_{0.07}Co_{0.2}Ce_{0.43}O_x$ observed in Figures 1d and S1 such that the APXPS measurement captures the properties of the catalytically active species at low overpotential.

Because the escaping photoelectrons can electrostatically interact with local fields, XPS provides information about the local potentials experienced by the atoms undergoing the photoionization process.[65,66] By measuring the core-level binding energy (BE) shift of the elements present in the liquid layer (e.g., O 1s or K 2p peaks) as a function of the applied potential at the WE, it is possible to achieve full potential control at the solid/liquid interface and monitor the ion-supported electrical connection between the electrolyte layer on the sample surface and the bulk liquid phase, as reported in Figure S2a,b.

The photoelectron peaks of Ce, Ni, and Co are shown in Figure 3a, b, and c, respectively, acquired in high vacuum (HV, 10^{-6} Torr), in the presence of water vapor (hydrated conditions, about 18 Torr), and under electrochemical conditions, both at the open circuit potential (OCP, −0.125 V vs $Ag/AgCl/Cl^-_{(sat.)}$) and at the selected OER overpotential (0.55 V vs $Ag/AgCl/Cl^-_{(sat.)}$). In the case of Ce, the photoionization process involving the 3d orbitals results in a rearrangement of the valence electrons. Due to the electrostatic interaction with the 3d core hole, the localized 4f levels

undergo a downward shift below the Fermi level, so that hybridizations with the O 2p band take place. Therefore, the Ce 3d orbitals, both in $Ce^{(III)}{}_2O_3$ and $Ce^{(IV)}O_2$, are constituted by multiplets derived from the $4f^0$-$4f^1$ and pure $4f^1$ final state configurations, respectively. The multipeak fitting procedure[67−70] reported in Figure 3a indicates the presence of Ce(III) in the pristine sample (green shaded areas), which is partially reoxidized upon exposure to water vapor (hydrated conditions), with the Ce(III) fraction decreasing from 19% to 11%. The remaining Ce(III) is completely oxidized after dipping the WE into the electrolyte, as no Ce(III) can be detected in the OCP measurement. Furthermore, no further changes are observed to the Ce 3d core level under catalytic conditions, confirming that the CeO_2 nanoparticles observed in ex situ nanocharacterization experiments[38] persist in the near-surface region under catalytic conditions.

The TM 2p core levels pose a number of complications in the fitting procedure, including shakeup, plasmon loss structures, and multiplet splitting. The former are responsible for the generation of additional satellite peaks,[71] usually characterized by a wide spectral broadening. On the other hand, multiplet splitting in the first-row TM arises from unpaired d electrons in the valence band and are usually associated with an oxygen-rich environment; in these instances, when a core electron vacancy is formed upon the photoionization process, there can be coupling between the unpaired 2p electrons in the core with the unpaired outer shell d electrons.[71] This can create a number of different final states, which will manifest in the photoelectron spectrum through additional spectral features. Nonetheless, other many-body processes influencing the core-hole lifetime can take place, such as Coster−Kronig transitions, which induce different full width at half-maximum (FWHM) values of the $2p_{3/2}$ and $2p_{1/2}$ core-level peaks.[71,72] An additional complication arises from the fact that the studied material was prepared through a nonselective synthetic route; thus, different oxidation states and structures (including nanosized crystallites[38]) are present at the surface, all contributing different amounts to the detected core levels. Finally, the energy resolution of the tender X-ray APXPS, about 0.3 eV, does not enable discrimination of spectral fine structures. For these reasons, we have developed an alternative fitting procedure. The Ni and Co $2p_{3/2}$ peaks are first compared to literature reference spectra[73] to isolate the main cation species responsible for the spectral line-shape. Then, the peaks are fit according to the literature procedure for the targeted cation.[73]

As can be seen in Figure 3b, the Ni 2p for the pristine material (analyzed in high vacuum) shows the typical line-shape of the rock-salt NiO structure, with Ni present as Ni(II).[73] Passing from the pristine material to the OCP conditions, the Ni $2p_{3/2}$ peak undergoes a positive shift of about 0.7 eV. Moreover, an important decrease of the satellites centered at about 856 and 861 eV takes place. These observations are consistent to the partial conversion of the $Ni^{(II)}O$ structure to $Ni^{(II)}(OH)_2$.[74] Similarly to the reports for other Ni-based systems,[54] Ni undergoes a partial oxidative conversion from Ni(II) to Ni(III) as a consequence of the formation of the active $Ni^{(III)}O(OH)$ phase under catalytic conditions (oxygen evolution). This is substantiated by the slight decrease (about 0.4 eV) of the binding energy of the Ni $2p_{3/2}$ peak from the OCP to the OER condition,[74] clearly observed in the difference spectrum at the top of Figure 3b. The complete conversion of the $Ni^{(II)}(OH)_2$/NiO system into the $Ni^{(III)}O(OH)$ phase should involve different initial and final state configurations, leading to a different Ni 2p shape (especially the 3/2 spectral contribution), and the importance of the partial conversion to $Ni^{(III)}O(OH)$ is discussed further below.[74]

Co exhibits a progressive evolution from a mixed oxide (Co_3O_4 or $Co^{(II)}O{\cdot}Co^{(III)}{}_2O_3$) in the pristine material to a mainly $Co^{(II)}(OH)_2$ structure[73] at the OCP, as substantiated by the positive BE shift of the overall peak (by about 0.7 eV) and the important increase of the Co(II) shake up satellite at about 786 eV.[75] This partial reductive conversion is usually ascribed to hydroxylation of the outer surface, which is due to the high concentration of hydroxyls in the electrolyte. Interestingly, at +550 mV versus $Ag/AgCl/Cl^-{}_{(sat.)}$, the $2p_{3/2}$ undergoes a downward BE shift, which is accompanied by significant spectral broadening. These changes are a clear fingerprint of the partial oxidation of $Co^{(II)}(OH)_2$ into a substoichiometric cobalt oxyhydroxide ($Co^{(II,III)}O_x(OH)_y$) species.[75] Previous studies of Co and Ni oxide-based materials have established a correlation between OER catalytic activity and the concomitant oxidation of $Co^{(II)}$ and $Ni^{(II)}$ to $Co^{(III)}$ and $Ni^{(III)}$, creating intrigue into the coexistence of these species in this low current density operation of $Ni_{0.3}Fe_{0.07}Co_{0.2}Ce_{0.43}O_x$, which is discussed below.[53−55]

To further understand the active species in this complex oxide catalysts, we perform complementary XAS experiments, which probe transitions from core-level electronic states to higher-energy unoccupied electronic states, showing sensitivity to oxidation state (similar to XPS), while also revealing details of the electronic structure of the material being observed.[76] Additionally, the EXAFS region of the spectrum provides short-range (<0.5 nm) structural information, making XAS a suitable tool for probing the interplay between bonding environment and electronic structure.[77,78] As discussed above, when using fluorescence detection, the probed depth (∼10 μm when resonant at 7 keV) is significantly higher than XPS, allowing investigation of the bulk properties of the entire catalyst film. The operando electrochemical cells used in this study take advantage of this large probe depth by introducing the X-rays through the back of the catalyst, avoiding the requirement for a thin electrolyte layer and any subsequent limitations to the electrochemical current density. Therefore, operando XAS is used to determine the catalyst behavior at higher overpotential and current density. Figure S1 d−f report the electrochemical characterization of the catalyst in 1.0 M KOH in the operando XAS cell, which includes the demonstration of stable electrocatalytic current density of approximately 8 mA cm^{-2} at 0.62 V vs $Ag/AgCl/Cl^-{}_{(sat.)}$, in approximate agreement with the 10 mA cm^{-2} previously observed in 1.0 M NaOH electrolyte.[37] This OER overpotential of approximately 0.41 V was chosen as the catalytic condition for XAS measurements due to the previous observation of comparable OER activity of $Ni_{0.3}Fe_{0.07}Co_{0.2}Ce_{0.43}O_x$ with optimal Ni−Fe catalysts at this potential.[37]

Ce L_3, Ni K, and Co K edges are shown in Figure 3d, e, and f, respectively, for the dry catalyst (pristine), at OCP (−135 mV vs $Ag/AgCl/Cl^-{}_{(sat.)}$), and under catalytic conditions (+620 mV vs $Ag/AgCl/Cl^-{}_{(sat.)}$). The Ce L_3 edge, shown in Figure 3d, remains constant under all measured conditions, thereby confirming that Ce is not redox active in the potential range under investigation and is present as CeO_2 under catalytic conditions.[79−81]

Ni and Co, however, both show clear redox activity passing from the OCP to catalytic conditions. The Ni K edge spectra

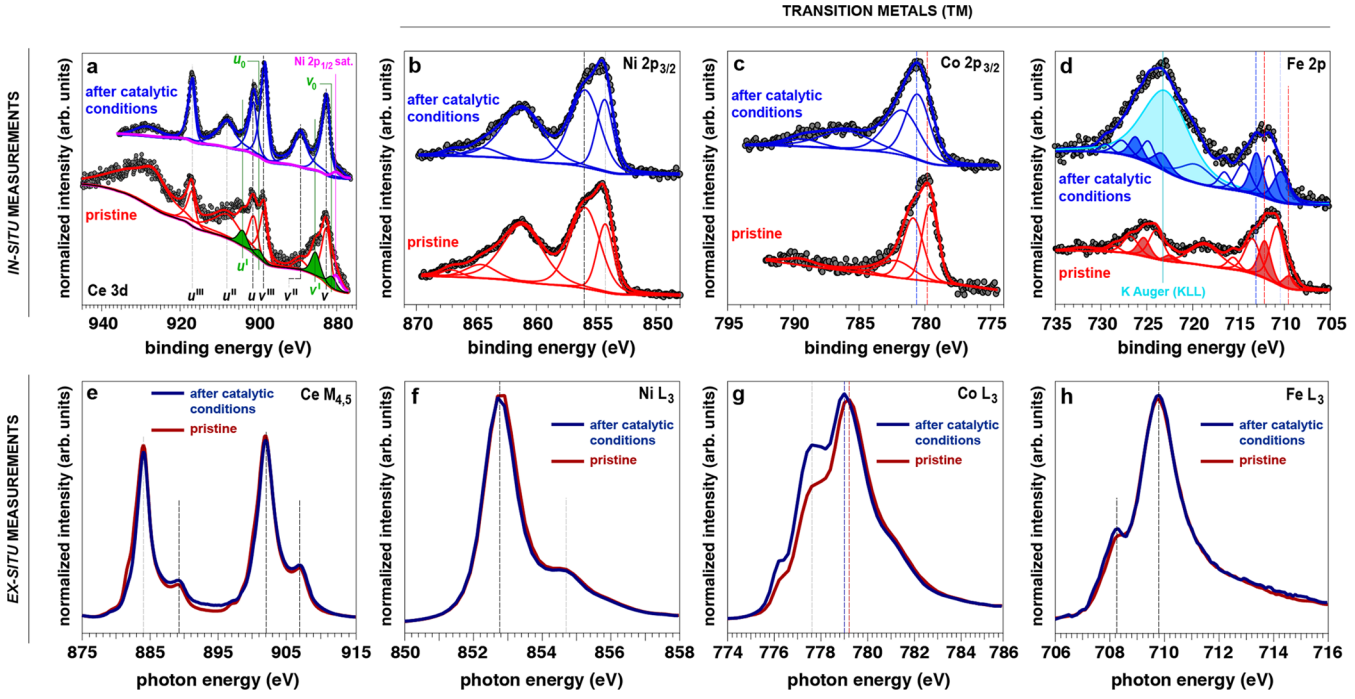

Figure 4. Top: in situ APXPS of the pristine material and after catalytic conditions (performed at 4000 eV and under hydrated conditions at a water vapor pressure between 16 and 18 Torr); (a) Ce 3d; (b) Ni $2p_{3/2}$; (c) Co $2p_{3/2}$; (d) Fe 2p. Bottom: ex situ XAS of the pristine material and after catalytic conditions, at the Ce $M_{4,5}$ (e) and at the Ni (f), Co (g), and Fe K edges (h).

(Figure 3e) are nearly identical for the pristine sample and at the OCP with a +1.65 eV shift under catalytic conditions, indicating partial oxidative conversion from $Ni^{(II)}$ to $Ni^{(III)}$. Operando EXAFS measurements (see SI Figure S3a,b) show a decrease in Ni−O bond lengths of ∼0.19 Å under catalytic conditions, consistent with Ni oxidation. The latter is significantly more pronounced than that observed by operando APXPS at low current density. This implies that at higher current densities, Ni becomes significantly more active in the quinary metal oxide catalyst and undergoes similar chemistry to $Ni_{1-x}Fe_x$ oxide catalysts under the same conditions. Friebel et al.[54] have demonstrated that, in $Ni_{1-x}Fe_x$ oxide catalysts, Ni undergoes a complete oxidation to Ni(III) under catalytic conditions, while Fe(III) occupies octahedral sites with a short Fe−O bond distance. The effect of this compression is that Fe(III) centers hosted in the $Ni^{(III)}{}_{1-x}Fe^{(III)}{}_xO(OH)$ structure become active toward water oxidation.[54] It is likely that the quinary metal oxide catalyst displays a similar catalytic mechanism at high current density.

At the Co K edge, shown in Figure 3f, a positive shift of +0.9 eV is observed when immersing the sample in the electrolyte, implying that some Co(II) in the pristine sample is oxidized to Co(III) immediately, before any potential is applied. Under catalytic conditions, a further shift of +0.6 eV is observed, as Co undergoes the previously discussed oxidative conversion to Co(III). While operando EXAFS does not show clear peak shifts under applied potential, the increase of overall peak intensity suggests more uniform Co−O and Co−Co bond lengths under catalytic conditions. This can be explained by oxidation of the Co(II) fraction in the initial state to Co(III). Assuming a mixed oxide phase similar to Co_3O_4, the octahedral Co(III) sites should display longer Co−O distances and shorter Co−X (X = Co, Ni, Fe) distances compared to tetrahedral Co(II) sites.[82] The change in distribution of bond lengths upon oxidation manifests as an overall sharpening of the EXAFS peaks as well as a slight skew to longer distance for the Co−O peak near 0.144 nm, and a slight skew toward shorter distance for the Co−X peak near 0.240 nm. The observed oxidation upon immersion in electrolyte is different from the behavior observed by operando APXPS, in which the starting Co_2O_3 or $Co^{(II)}O{\cdot}Co^{(III)}{}_2O_3$ is partially reduced at the outer surface to $Co^{(II)}(OH)_2$ upon immersion in the electrolyte. No evidence for $Co^{(II)}(OH)_2$ is seen in the Co K edge XAS spectra, suggesting that this species is only formed in the outer surface layer of the film, while the bulk is likely still a mixed oxide $Co^{(II)}O{\cdot}Co^{(III)}{}_2O_3$, with the Co(III) fraction increasing when immersed in electrolyte. Under catalytic conditions, however, the spectral shift is consistent with XPS results, which show partial oxidation to a final substoichometric cobalt oxyhydroxide ($Co^{(II,III)}O_x(OH)_y$) species. In addition, a similar Co XANES shift has been observed in different cobalt-based electrocatalysts in literature between OCP and oxygen evolution conditions.[56,82−85] This shift has been interpreted as the formation of a Co(IV) fraction at catalytic conditions, following a Co(II) → Co(III) → Co(IV) redox scheme. The EXAFS spectrum collected under the catalytic condition (SI, Figure S3a) also resembles the one reported by Kanan et al.[56]

Therefore, we hypothesize the presence of a mixed configuration at the surface at high current densities (∼8 mA cm^{-2}), where we observe the partial oxidative conversion to cobalt oxyhydroxide (Co(II) → Co(III)) and the presence of Co(IV) (Co(III) → Co(IV)) as an active species in the catalytic cycle.[56,82−85] The relatively small spectral shift observed by XAS is consistent with conversion being limited to the near-surface region. On the other hand, at the lower current densities (up to 1 mA cm^{-2}) probed by operando APXPS, the steady-state concentration of Co(IV) seems to be below the detection limit.

Regarding the redox chemistry of Fe, the small concentration of Fe in the catalyst and Fe contaminants homogeneously

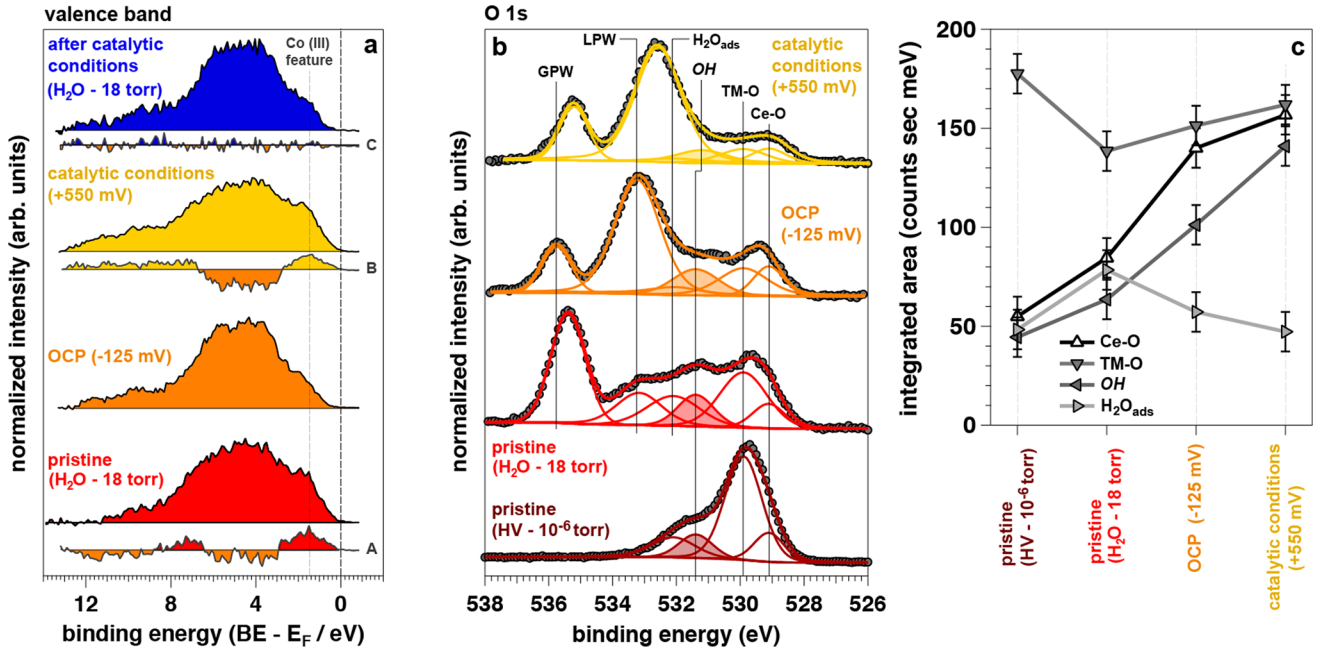

Figure 5. (a) Background subtracted and area normalized valence band (VB) of the quinary metal oxide catalyst under operando and resting conditions, at a photon energy of 4000 eV. The difference spectra A, B, and C have been obtained using the VB at OCP as reference; (b,c) Multipeak fitting procedure performed on the O 1s peak (acquired at 4000 eV) and trend of the integrated areas of the fitting components as a function of the different investigated conditions, respectively. The fitting components were normalized for the effective attenuation length (EAL) of the liquid layer on the sample surface using the inverse Beer–Lambert relation. The potentials are with respect to the $Ag/AgCl/Cl^-_{(sat.)}$ reference electrode.

present in the glassy carbon substrate unfortunately precludes any observation of activity at the Fe sites via the Fe K edge XAS.

To characterize the reversibility of the observed redox processes, post mortem analysis of $Ni_{0.3}Fe_{0.07}Co_{0.2}Ce_{0.43}O_x$ was performed after 3 h of OER electrocatalysis at about 1 mA cm^{-2} (see Figure S1c), using in situ APXPS and ex situ soft X-ray XAS (Figure 4). Soft X-ray XAS (photon energies <2 keV) probes a complementary set of core-level excitations, providing additional information about electronic and bonding environment, but lower penetration depths necessitate ultrahigh vacuum conditions. This energy range gives access to the $L_{2,3}$ and $M_{4,5}$ edge spectra for Fe, Co, Ni, and Ce, respectively, which are highly sensitive to oxidation state, spin state, and coordination structure.[86,87] All of these spectra are obtained using total electron yield (TEY) detection, which has a probe depth of only a few nm and is therefore directly comparable to XPS.[88] By measuring both pristine samples and samples that have been subjected to the catalytic conditions, any changes to the electronic and atomic structure as a result of the catalytic chemistry can be observed.

The in situ APXPS survey scans (BE: 0–1000 eV) acquired at 4000 eV on the pristine material and after catalytic conditions are reported in Figure S4, whereas the high-resolution measurements of the elemental spectral regions of interest and the corresponding soft-X-ray TEY edges are reported in Figure 4. The analysis of the Ce 3d core level (Figure 4a) reveals that Ce remains exclusively as Ce(IV) in the common CeO_2 fluorite structure in the post mortem catalyst. Ex situ Ce M and TM L edge spectra of the catalyst before and after electrochemistry are shown in Figure 4e and 4f, g, and h, respectively. No significant spectral changes are observed at the Ce $M_{4,5}$ edge, shown in Figure 4e, with the spectra for catalysts before and after electrochemistry both matching that of $Ce^{(IV)}O_2$. A small shoulder at 881.4 eV, however, may indicate a small amount of $Ce^{(III)}$ in the pristine sample,[89,90] as seen in the APXPS measurements.

The observed redox states of Ni species in the operando measurements are found to be completely reversible, as Ni is present as $Ni^{(II)}O$ with no evidence for any $Ni^{(III)}$ species in both the pristine and post mortem catalysts (Figure 4b,f).[91] Regarding the chemistry of Co, from the XPS data reported in Figure 4c, it is possible to observe the presence of $Co^{(II)}(OH)_2$, but not of $Co^{(III)}O(OH)$, in the post mortem sample.[75] The Co L_3 edge spectrum of the pristine catalyst, shown in Figure 4g, is similar to that of the mixed oxide $Co^{(II, III)}{}_3O_4$, but the increased intensity of the feature near 777.8 eV, as well as the appearance of a new feature near 776.3 eV, indicates a higher concentration of $Co^{(II)}$.[92] After electrochemistry, these two features are further increased in intensity, and the spectrum resembles that of $Co^{(II)}(OH)_2$, indicating reversibility of the charge state in the electrochemical redox processes with retention of hydroxyls. For both Ni and Co, the catalytically active species are labile, with $Ni^{(III)}O(OH)$ and $Co^{(III)}O(OH)$ observed exclusively under operando conditions.

Unlike other elements in the quinary metal oxide, the APXPS analysis of the minority Fe species is limited to the pristine and cycled material because of its small concentration. The coupling between the low Fe content and the attenuation imposed by the liquid layer and the relatively high-pressure environment (about 18 Torr) for the ejected photoelectrons, precluded detection of Fe under operando conditions. Comparison of the Fe 2p photoemission peaks for the pristine and cycled material reported in Figure 4d indicates that Fe undergoes an oxidation from a mixed Fe_3O_4 ($Fe^{(II)}O{\cdot}Fe_2^{(III)}O_3$) system to a mainly Fe(III)-based structure.[73] Fe(III) is actually the main oxidation state of Fe in the cycled sample, as substantiated by the positive BE shift of the overall Fe 2p peak (about 0.9 eV)[93] and the

significant increase of the doublets whose 3/2 components are centered at about 710.4 and 713.1 eV (shadowed areas in Figure 4d). Unambiguous determination of the particular structure present at the surface is not possible because of the spectral overlap of the different Fe(III) phases. From comparison with other reports, we hypothesize the presence of Fe(III) in $Ni^{(III)}_{1-x}Fe^{(III)}_{x}O(OH)$[54,93,94] and $Fe_2{}^{(III)}O_3$[95] resulting from restructuring of the surface upon removal of the anodic potential. The Fe L_3 edge spectrum of the pristine catalyst, shown in Figure 4h, is between that of $Fe^{(II)}O$ and $Fe^{(II,III)}{}_3O_4$, indicating a mixed oxide phase containing both Fe(II) and Fe(III).[96] After catalytic conditions, the spectrum is essentially unchanged. A slight sharpening of the feature near 708.3 eV is consistent with an oxidation state of Fe(III) at the surface, as observed by in situ APXPS. Unfortunately, the spectra of Fe(III) in different structural environments are nearly identical,[96,97] making an exact determination of which species are present at the surface difficult. A mixture of Fe(III) in $Ni^{(III)}_{1-x}Fe^{(III)}_{x}O(OH)$ and $Fe_2{}^{(III)}O_3$, as inferred from in situ APXPS, is likely. These observations agree with previous work conducted on Fe−Ni- and Fe−Co-based materials, where the Fe(III) species formed under operational conditions exhibit high activity for the OER, and it is worth noting that Fe(III) species form at lower potentials than the Ni and Co redox processes described above.[93]

To gain further insight into the electronic properties of the quinary transition metal catalyst, the valence band (VB) XPS was acquired on the pristine material (hydrated conditions, 16 Torr), under operando conditions (at the OCP and at 0.55 V vs $Ag/AgCl/Cl^-_{(sat.)}$), and "post mortem" after 3 h of oxygen evolution (hydrated conditions, 16 Torr). The results are reported in Figure 5.

The VB, as observed in Figures 5a, consists of three different regions, which can be identified by their position with respect to the Fermi level (normalized to zero via the tangent method and the calibration of O 2s, at around 23 eV). The first region, within the first 3 eV below the Fermi level, is constituted by the density of states (DOS) at the upper edge of the VB. Typically these states are generated by low-energy hybridizations of the metal valence shells (in this case, the 4f from Ce and the 3d from Ni, Co, and Fe). The states that fall in this region are mainly responsible for the catalytic activity and electrical conductivity properties of the material, through their partial hybridization with states localized at the lower edge of the conduction band (CB) or localized states introduced in the energy band gap by a dopant. The second region, between 3 and 7 eV below the Fermi level is typical of the metal oxides and, in this case, is generated by the hybridization of the O 2p orbitals with the Ce 4f and Ni, Co, Fe 3d states. Finally, above 8 eV, hybridization between the O 2p and 2s shells from adsorbed and multilayer water on the surface occurs.[98,99]

In the first VB region of the pristine material and under operando OER conditions, it is possible to observe the $(t_{2g})^5$ final state feature of Co(III) (d^6, centered at 1.5 eV below the Fermi level), confirming the results discussed above about the core-level photoemission of Co.[75,100] This is also in line with the observations of Weidler et al. on Co-based electrocatalysts prepared using a CVD procedure.[75] In agreement with the core-level spectroscopy, the VB Co(III) feature is weaker at the OCP and post mortem conditions due to the partial reductive conversion of $Co^{(II,III)}{}_3O_4$ and $Co^{(II,III)}O_x(OH)_y$ into $Co^{(II)}(OH)_2$, respectively.

The partial oxidation of Ni and Co during the catalytic conditions is also confirmed by the analysis of the O 1s photoelectron peak, reported in Figures 5b,c (specifically by the trend of the TM-O^{2-} and OH components as a function of the different conditions). In particular, it is possible to observe that the hydroxyl component undergoes a negative shift by about 0.3 eV when the material is under catalytic conditions. This is in agreement with other studies in literature, showing that the formation of the catalytic phases $Ni^{(III)}O(OH)$ and $Co^{(III)}O(OH)$ leads to a downward shift of the OH BE component, as a result of the strong negative crystalline fields in the oxohydroxide trivalent TM compounds.[75] Moreover, a full conversion from a $(Ni,Co,Fe)^{(II)}(OH)_2$ to a $(Ni,Co,Fe)^{(III)}O(OH)$ phase should lead to a higher negative shift of the OH BE component (~1.1 eV) compared to that observed in this study.[75] This observation is in line with the previous discussion regarding the partial oxidative conversion of Ni and Co at low overpotential/low current density operation (0.55 V vs $Ag/AgCl/Cl^-_{(sat.)}$ and ~1 mA cm^{-2}).

As noted above, complete oxidation of Fe into Fe(III) is expected at this potential, and given the high activity of Fe(III) species,[93] its small concentration in the quinary oxide catalyst may play a role in optimization of OER activity. While the CeO_2 may play a variety of roles in catalyst optimization, including structural scaffolding, the present work establishes perhaps its most important role in catalyst optimization. Its chemical influence on the other cations is revealed through the observations that CeO_2 mediates the introduction of transition-metal redox activity at low overpotential and that only a fraction of near-surface Ni and Co atoms are oxidized into active Ni(III) and Co(III) species in the low overpotential catalyst operation where the quinary oxide was found to exhibit unique, superior activity. Table S2 includes a summary of the operando species observed in $Ni_{0.3}Fe_{0.07}Co_{0.2}Ce_{0.43}O_x$ with comparisons to literature reports on Ni-, Fe-, and Co-based catalysts.

CONCLUSIONS

The operando APXPS findings suggest that at low current densities the electrochemical performance of the quinary metal oxide is supported by Ni, Co, and Fe, specifically on their electrochemical activation from a II oxidation state to active $(Ni,Fe,Co)^{(III)}O(OH)$ species, albeit a partial oxidation in the case of Ni and Co. The operando XAS results highlight similarities and differences in the catalytic mechanism under low (~1 mA/cm^2) and high (~8 mA/cm^2) current density regimes. While in situ and ex situ surface analyses demonstrate the presence of Fe(III) species both before and after catalyst operation, the redox activity of Ni and Co near the onset of catalytic activity is critical to catalyst operation and optimization. At high current density, Ni is highly active in the catalyst and is reversibly oxidized from $Ni^{(II)}O$ to $Ni^{(III)}O(OH)$ under catalytic conditions, as seen in similar $Ni_{1-x}Fe_x$ catalysts, whereas at low current density only limited amounts of $Ni^{(III)}O(OH)$ are detected by operando APXPS. The bulk behavior of Co in the catalyst is significantly different than that at the surface, displaying partial bulk oxidation from Co(II) to Co(III) upon immersion in the electrolyte, likely through changing composition of the mixed $Co^{(II)}O{\cdot}Co^{(III)}{}_2O_3$ phase. The surface is actually reduced to $Co^{(II)}(OH)_2$ upon immersion in the electrolyte and then partially oxidized to a substoichiometric cobalt oxyhydroxide ($Co^{(II,III)}O_x(OH)_y$) at low-overpotential catalytic conditions with further oxidation

observed at higher overpotential. At the higher overpotential, this $Co^{(III)}O(OH)$ layer persists deep enough into the catalyst film to be observed by fluorescence yield XAS. In addition, at the explored current density (~8 mA cm^{-2}), our XAS results resemble the data reported in literature about the existence of Co(IV) as active centers in cobalt-based electrocatalysts for oxygen evolution.

As reported, a detailed analysis of the role of Fe on the overall catalyst performance could not be achieved in an operando fashion. On the other hand, ex situ investigations have shown that Fe is mainly present as Fe(III) after catalytic conditions. Therefore, we can conclude that Fe is activated in the material at the potentials explored in the work, most likely as Fe(III) hosted in octahedral sites in $Ni^{(III)}_{1-x}Fe^{(III)}_{x}O(OH)$, as reported in literature for $Ni_{1-x}Fe_x$ catalysts.[87]

Although a detailed explanation of the catalytic mechanism involving the oxidation states of the TMs is still to be determined, our findings allow us to conclude that the TM oxyhydroxide phases are promoted under catalytic conditions and synergistically cooperate to enable the observed high electroactivity of water oxidation. In particular, our study shows that the direct observation of the activated species and the differences between high and low overpotential operation are possible only under operando conditions, particularly because the redox chemistry of TMs is largely reversible.

These results reveal an indirect influence of CeO_2 on catalytic activity wherein the active species are the same transition metal oxyhydroxides observed in Ce-free catalysts and form at lower overpotentials due to interactions with nanocrystalline CeO_2. Given the partial conversion to these species at the low current density condition where $Ni_{0.3}Fe_{0.07}Co_{0.2}Ce_{0.43}O_x$ exhibits uniquely high activity, the oxyhydroxide species may be limited to the Ni and Co atoms in close proximity to the CeO_2, implying that the previously observed atomically sharp grain boundaries are an important factor in the performance of this complex oxide catalyst and in boosting the water oxidation kinetics. This proposed role of CeO_2 is reminiscent of, and more subtle than, the spillover effect of Pt-based ORR electrocatalysts, indicating that nanocrystalline CeO_2 may continue to be a critical component of optimized catalysts for both the ORR and OER.

■ ASSOCIATED CONTENT

Supporting Information

The Supporting Information is available free of charge on the ACS Publications website at DOI: 10.1021/acscatal.6b03126.

Experimental details of samples preparation and synchrotron-based operando APXPS and XAS, electrochemical characterization of the $Ni_{0.3}Fe_{0.07}Co_{0.2}Ce_{0.43}O_x$ catalysts under operando APXPS and XAS experimental conditions, operando APXPS conductivity measurements of the nanometer thick electrolyte layer for operando APXPS experiments, operando EXAFS at the Co and Ni K edges obtained under catalytic conditions, in situ APXPS survey scans for the qualitative identification of the surface chemistry of the $Ni_{0.3}Fe_{0.07}Co_{0.2}Ce_{0.43}O_x$ catalyst before and after catalytic conditions, and comparative table reporting the results obtained in this work together with previous literature findings (PDF)

■ AUTHOR INFORMATION

Corresponding Authors

*E-mail: ejcrumlin@lbl.gov.
*E-mail: jahaber@caltech.edu.
*E-mail: jyano@lbl.gov.

ORCID

John M. Gregoire: 0000-0002-2863-5265
Junko Yano: 0000-0001-6308-9071

Author Contributions

¶These two authors equally contributed to the work (M.F. and W.S.D.).

Notes

The authors declare no competing financial interest.

■ ACKNOWLEDGMENTS

We thank Dan Guevarra for his assistance collecting the cyclic voltamograms shown in Figure 1, using the scanning drop electrochemical cell. This material is based upon work performed by the Joint Center for Artificial Photosynthesis, a DOE Energy Innovation Hub, supported through the Office of Science of the U.S. Department of Energy (Award No. DE-SC0004993). The XAS work was done at BL 10.3.2 at the Advanced Light Source, and at BL 7-3 at the Stanford Synchrotron Radiation Lightsource. The APXPS work was done at BL 9.3.1 at the Advanced Light Source. Use of the Stanford Synchrotron Radiation Lightsource, SLAC National Accelerator Laboratory, is supported by the U.S. Department of Energy, Office of Science, Office of Basic Energy Sciences under Contract No. DE-AC02-76SF00515. The Advanced Light Source is supported by the Director, Office of Science, Office of Basic Energy Sciences, of the U.S. Department of Energy under Contract No. DE-AC02-05CH11231.

■ REFERENCES

(1) Cook, T. R.; Dogutan, D. K.; Reece, S. Y.; Surendranath, Y.; Teets, T. S.; Nocera, D. G. *Chem. Rev.* **2010**, *110*, 6474−6502.
(2) Katsounaros, I.; Cherevko, S.; Zeradjanin, A. R.; Mayrhofer, K. J. J. *Angew. Chem., Int. Ed.* **2014**, *53*, 102−121.
(3) Walter, M. G.; Warren, E. L.; McKone, J. R.; Boettcher, S. W.; Mi, Q. X.; Santori, E. A.; Lewis, N. S. *Chem. Rev.* **2010**, *110*, 6446−6473.
(4) Bell, A. T. *Science* **2003**, *299*, 1688−1691.
(5) Michalak, W. D.; Somorjai, G. A. *Top. Catal.* **2013**, *56*, 1611−1622.
(6) Schlogl, R.; Abd Hamid, S. B. *Angew. Chem., Int. Ed.* **2004**, *43*, 1628−1637.
(7) Yoon, C.; Cocke, D. L. *J. Non-Cryst. Solids* **1986**, *79*, 217−245.
(8) May, K. J.; Carlton, C. E.; Stoerzinger, K. A.; Risch, M.; Suntivich, J.; Lee, Y. L.; Grimaud, A.; Shao-Horn, Y. *J. Phys. Chem. Lett.* **2012**, *3*, 3264−3270.
(9) Smith, R. D. L.; Prevot, M. S.; Fagan, R. D.; Zhang, Z. P.; Sedach, P. A.; Siu, M. K. J.; Trudel, S.; Berlinguette, C. P. *Science* **2013**, *340*, 60−63.
(10) Zhang, C.; Trudel, S.; Berlinguette, C. P. *Eur. J. Inorg. Chem.* **2014**, *2014*, 660−664.
(11) Indra, A.; Menezes, P. W.; Sahraie, N. R.; Bergmann, A.; Das, C.; Tallarida, M.; Schmeißer, D.; Strasser, P.; Driess, M. *J. Am. Chem. Soc.* **2014**, *136*, 17530−17536.
(12) Yang, Y.; Fei, H. L.; Ruan, G. D.; Xiang, C. S.; Tour, J. M. *ACS Nano* **2014**, *8*, 9518−9523.
(13) Iyer, A.; Del-Pilar, J.; King'ondu, C. K.; Kissel, E.; Garces, H. F.; Huang, H.; El-Sawy, A. M.; Dutta, P. K.; Suib, S. L. *J. Phys. Chem. C* **2012**, *116*, 6474−6483.
(14) Kanan, M. W.; Nocera, D. G. *Science* **2008**, *321*, 1072−1075.
(15) Qiu, Y.; Xin, L.; Li, W. Z. *Langmuir* **2014**, *30*, 7893−7901.

(16) Chemelewski, W. D.; Lee, H.-C.; Lin, J.-F.; Bard, A. J.; Mullins, C. B. *J. Am. Chem. Soc.* **2014**, *136*, 2843−2850.
(17) Muller, C. I.; Rauscher, T.; Schmidt, A.; Schubert, T.; Weissgarber, T.; Kieback, B.; Rontzsch, L. *Int. J. Hydrogen Energy* **2014**, *39*, 8926−8937.
(18) Klingan, K.; Ringleb, F.; Zaharieva, I.; Heidkamp, J.; Chernev, P.; Gonzalez-Flores, D.; Risch, M.; Fischer, A.; Dau, H. *ChemSusChem* **2014**, *7*, 1301−1310.
(19) Pajonk, G. M. *Appl. Catal., A* **2000**, *202*, 157−169.
(20) Weng, L. T.; Delmon, B. *Appl. Catal., A* **1992**, *81*, 141−213.
(21) Conner, W. C.; Falconer, J. L. *Chem. Rev.* **1995**, *95*, 759−788.
(22) Corrigan, D. A.; Conell, R. S.; Fierro, C. A.; Scherson, D. A. *J. Phys. Chem.* **1987**, *91*, 5009−5011.
(23) Corrigan, D. A.; Bendert, R. M. *J. Electrochem. Soc.* **1989**, *136*, 723−728.
(24) Subbaraman, R.; Tripkovic, D.; Chang, K. C.; Strmcnik, D.; Paulikas, A. P.; Hirunsit, P.; Chan, M.; Greeley, J.; Stamenkovic, V.; Markovic, N. M. *Nat. Mater.* **2012**, *11*, 550−557.
(25) Lyons, M. E. G.; Doyle, R. L.; Fernandez, D.; Godwin, I. J.; Browne, M. P.; Rovetta, A. *Electrochem. Commun.* **2014**, *45*, 56−59.
(26) Lyons, M. E. G.; Doyle, R. L.; Fernandez, D.; Godwin, I. J.; Browne, M. P.; Rovetta, A. *Electrochem. Commun.* **2014**, *45*, 60−62.
(27) Dionigi, F.; Strasser, P. *Adv. Energy Mater.* **2016**, *6*, 1600621.
(28) Corrigan, D. A. *J. Electrochem. Soc.* **1987**, *134*, 377−384.
(29) Smith, A. M.; Trotochaud, L.; Burke, M. S.; Boettcher, S. W. *Chem. Commun.* **2015**, *51*, 5261−5263.
(30) Trotochaud, L.; Boettcher, S. W. *Scr. Mater.* **2014**, *74*, 25−32.
(31) Trotochaud, L.; Young, S. L.; Ranney, J. K.; Boettcher, S. W. *J. Am. Chem. Soc.* **2014**, *136*, 6744−6753.
(32) Lin, F. D.; Bachman, B. F.; Boettcher, S. W. *J. Phys. Chem. Lett.* **2015**, *6*, 2427−2433.
(33) Nellist, M. R.; Laskowski, F. A. L.; Lin, F. D.; Mills, T. J.; Boettcher, S. W. *Acc. Chem. Res.* **2016**, *49*, 733−740.
(34) Burke, M. S.; Enman, L. J.; Batchellor, A. S.; Zou, S. H.; Boettcher, S. W. *Chem. Mater.* **2015**, *27*, 7549−7558.
(35) Burke, M. S.; Zou, S. H.; Enman, L. J.; Kellon, J. E.; Gabor, C. A.; Pledger, E.; Boettcher, S. W. *J. Phys. Chem. Lett.* **2015**, *6*, 3737−3742.
(36) Enman, L. J.; Burke, M. S.; Batchellor, A. S.; Boettcher, S. W. *ACS Catal.* **2016**, *6*, 2416−2423.
(37) Haber, J. A.; Cai, Y.; Jung, S. H.; Xiang, C. X.; Mitrovic, S.; Jin, J.; Bell, A. T.; Gregoire, J. M. *Energy Environ. Sci.* **2014**, *7*, 682−688.
(38) Haber, J. A.; Anzenburg, E.; Yano, J.; Kisielowski, C.; Gregoire, J. M. *Adv. Energy Mater.* **2015**, *5*, 1402307.
(39) Haber, J. A.; Xiang, C.; Guevarra, D.; Jung, S.; Jin, J.; Gregoire, J. M. *ChemElectroChem* **2014**, *1*, 524−528.
(40) Cargnello, M.; Doan-Nguyen, V. V. T.; Gordon, T. R.; Diaz, R. E.; Stach, E. A.; Gorte, R. J.; Fornasiero, P.; Murray, C. B. *Science* **2013**, *341*, 771−773.
(41) Trovarelli, A. *Catal. Rev.: Sci. Eng.* **1996**, *38*, 439−520.
(42) Zafiris, G. S.; Gorte, R. J. *J. Catal.* **1993**, *139*, 561−567.
(43) Lee, W.; Jung, H. J.; Lee, M. H.; Kim, Y. B.; Park, J. S.; Sinclair, R.; Prinz, F. B. *Adv. Funct. Mater.* **2012**, *22*, 965−971.
(44) Vayssilov, G. N.; Lykhach, Y.; Migani, A.; Staudt, T.; Petrova, G. P.; Tsud, N.; Skala, T.; Bruix, A.; Illas, F.; Prince, K. C.; Matolin, V.; Neyman, K. M.; Libuda, J. *Nat. Mater.* **2011**, *10*, 310−315.
(45) Ng, J. W. D.; García-Melchor, M.; Bajdich, M.; Chakthranont, P.; Kirk, C.; Vojvodic, A.; Jaramillo, T. F. *Nat. Energy* **2016**, *1*, 16053.
(46) Kwon, K.; Lee, K. H.; Jin, S. A.; You, D. J.; Pak, C. *Electrochem. Commun.* **2011**, *13*, 1067−1069.
(47) Lim, D. H.; Lee, W. D.; Choi, D. H.; Kwon, H. H.; Lee, H. I. *Electrochem. Commun.* **2008**, *10*, 592−596.
(48) Lim, D. H.; Lee, W. D.; Choi, D. H.; Lee, H. I. *Appl. Catal., B* **2010**, *94*, 85−96.
(49) Yu, H. B.; Kim, J. H.; Lee, H. I.; Scibioh, M. A.; Lee, J.; Han, J.; Yoon, S. P.; Ha, H. Y. *J. Power Sources* **2005**, *140*, 59−65.
(50) Fugane, K.; Mori, T.; Ou, D. R.; Suzuki, A.; Yoshikawa, H.; Masuda, T.; Uosaki, K.; Yamashita, Y.; Ueda, S.; Kobayashi, K.; Okazaki, N.; Matolinova, I.; Matolin, V. *Electrochim. Acta* **2011**, *56*, 3874−3883.
(51) Masuda, T.; Fukumitsu, H.; Fugane, K.; Togasaki, H.; Matsumura, D.; Tamura, K.; Nishihata, Y.; Yoshikawa, H.; Kobayashi, K.; Mori, T.; Uosaki, K. *J. Phys. Chem. C* **2012**, *116*, 10098−10102.
(52) Montini, T.; Melchionna, M.; Monai, M.; Fornasiero, P. *Chem. Rev.* **2016**, *116*, 5987−6041.
(53) Friebel, D.; Bajdich, M.; Yeo, B. S.; Louie, M. W.; Miller, D. J.; Sanchez Casalongue, H. G.; Mbuga, F.; Weng, T. C.; Nordlund, D.; Sokaras, D.; Alonso-Mori, R.; Bell, A. T.; Nilsson, A. *Phys. Chem. Chem. Phys.* **2013**, *15*, 17460−17467.
(54) Friebel, D.; Louie, M. W.; Bajdich, M.; Sanwald, K. E.; Cai, Y.; Wise, A. M.; Cheng, M. J.; Sokaras, D.; Weng, T. C.; Alonso-Mori, R.; Davis, R. C.; Bargar, J. R.; Norskov, J. K.; Nilsson, A.; Bell, A. T. *J. Am. Chem. Soc.* **2015**, *137*, 1305−1313.
(55) Gul, S.; Ng, J. W. D.; Alonso-Mori, R.; Kern, J.; Sokaras, D.; Anzenberg, E.; Lassalle-Kaiser, B.; Gorlin, Y.; Weng, T. C.; Zwart, P. H.; Zhang, J. Z.; Bergmann, U.; Yachandra, V. K.; Jaramillo, T. F.; Yano, J. *Phys. Chem. Chem. Phys.* **2015**, *17*, 8901−8912.
(56) Kanan, M. W.; Yano, J.; Surendranath, Y.; Dinca, M.; Yachandra, V. K.; Nocera, D. G. *J. Am. Chem. Soc.* **2010**, *132*, 13692−13701.
(57) Yoshida, M.; Gon, N.; Maeda, S.; Mineo, T.; Nitta, K.; Kato, K.; Nitani, H.; Abe, H.; Uruga, T.; Kondoh, H. *Chem. Lett.* **2014**, *43*, 1725−1727.
(58) Yoshida, M.; Kondoh, H. *Chem. Rec.* **2014**, *14*, 806−818.
(59) Yoshida, M.; Yomogida, T.; Mineo, T.; Nitta, K.; Kato, K.; Masuda, T.; Nitani, H.; Abe, H.; Takakusagi, S.; Uruga, T.; Asakura, K.; Uosaki, K.; Kondoh, H. *J. Phys. Chem. C* **2014**, *118*, 24302−24309.
(60) Wang, D.; Zhou, J.; Hu, Y.; Yang, J.; Han, N.; Li, Y.; Sham, T.-K. *J. Phys. Chem. C* **2015**, *119*, 19573−19583.
(61) Lichterman, M. F.; Hu, S.; Richter, M. H.; Crumlin, E. J.; Axnanda, S.; Favaro, M.; Drisdell, W.; Hussain, Z.; Mayer, T.; Brunschwig, B. S.; Lewis, N. S.; Liu, Z.; Lewerenz, H. J. *Energy Environ. Sci.* **2015**, *8*, 2409−2416.
(62) Lichterman, M. F.; Richter, M. H.; Hu, S.; Crumlin, E. J.; Axnanda, S.; Favaro, M.; Drisdell, W.; Hussain, Z.; Brunschwig, B. S.; Lewis, N. S.; Liu, Z.; Lewerenz, H. J. *J. Electrochem. Soc.* **2016**, *163*, H139−H146.
(63) Axnanda, S.; Crumlin, E. J.; Mao, B. H.; Rani, S.; Chang, R.; Karlsson, P. G.; Edwards, M. O. M.; Lundqvist, M.; Moberg, R.; Ross, P.; Hussain, Z.; Liu, Z. *Sci. Rep.* **2015**, *5*, Article No.9788.
(64) Lewerenz, H.-J.; Lichterman, M. F.; Richter, M. H.; Crumlin, E. J.; Hu, S.; Axnanda, S.; Favaro, M.; Drisdell, W.; Hussain, Z.; Brunschwig, B. S.; Liu, Z.; Nilsson, A.; Bell, A. T.; Lewis, N. S.; Friebel, D. *Electrochim. Acta* **2016**, *211*, 711−719.
(65) Fadley, C. S. *J. Electron Spectrosc. Relat. Phenom.* **2010**, *178-179*, 2−32.
(66) Starr, D. E.; Liu, Z.; Havecker, M.; Knop-Gericke, A.; Bluhm, H. *Chem. Soc. Rev.* **2013**, *42*, 5833−5857.
(67) Artiglia, L.; Agnoli, S.; Paganini, M. C.; Cattelan, M.; Granozzi, G. *ACS Appl. Mater. Interfaces* **2014**, *6*, 20130−20136.
(68) Luches, P.; Pagliuca, F.; Valeri, S. *J. Phys. Chem. C* **2011**, *115*, 10718−10726.
(69) Skala, T.; Sutara, F.; Prince, K. C.; Matolin, V. *J. Electron Spectrosc. Relat. Phenom.* **2009**, *169*, 20−25.
(70) Tsunekawa, S.; Fukuda, T.; Kasuya, A. *Surf. Sci.* **2000**, *457*, L437−L440.
(71) Becker, U.; Shirley, D. A. *VUV and Soft X-Ray Photoionization*; Springer: New York, 1996.
(72) Nyholm, R.; Martensson, N.; Lebugle, A.; Axelsson, U. *J. Phys. F: Met. Phys.* **1981**, *11*, 1727−1733.
(73) Biesinger, M. C.; Payne, B. P.; Grosvenor, A. P.; Lau, L. W. M.; Gerson, A. R.; Smart, R. S. *Appl. Surf. Sci.* **2011**, *257*, 2717.
(74) Biesinger, M. C.; Lau, L. W. M.; Gerson, A. R.; Smart, R. S. C. *Phys. Chem. Chem. Phys.* **2012**, *14*, 2434−2442.
(75) Weidler, N.; Paulus, S.; Schuch, J.; Klett, J.; Hoch, S.; Stenner, P.; Maljusch, A.; Brotz, J.; Wittich, C.; Kaiser, B.; Jaegermann, W. *Phys. Chem. Chem. Phys.* **2016**, *18*, 10708−10718.

(76) Koningsberger, D.; Prins, R. *X-ray absorption: principles, applications, techniques of EXAFS, SEXAFS, and XANES*; John Wiley & Sons: Hoboken, NJ, 1988.
(77) Teo, B. K. *EXAFS: Basic Principles and Data Analysis*; Springer: New York, 1986.
(78) Koningsberger, D.; Mojet, B.; Van Dorssen, G.; Ramaker, D. *Top. Catal.* **2000**, *10*, 143−155.
(79) Shahin, A. M.; Grandjean, F.; Long, G. J.; Schuman, T. P. *Chem. Mater.* **2005**, *17*, 315.
(80) Kaindl, G.; Schmiester, G.; Sampathkumaran, E. V.; Wachter, P. *Phys. Rev. B: Condens. Matter Mater. Phys.* **1988**, *38*, 10174−10177.
(81) Dexpert, H.; Karnatak, R. C.; Esteva, J. M.; Connerade, J. P.; Gasgnier, M.; Caro, P. E.; Albert, L. *Phys. Rev. B: Condens. Matter Mater. Phys.* **1987**, *36*, 1750−1753.
(82) McAlpin, J. G.; Surendranath, Y.; Dincă, M.; Stich, T. A.; Stoian, S. A.; Casey, W. H.; Nocera, D. G.; Britt, R. D. *J. Am. Chem. Soc.* **2010**, *132*, 6882−6883.
(83) Zhang, M.; de Respinis, M.; Frei, H. *Nat. Chem.* **2014**, *6*, 362−367.
(84) Risch, M.; Ringleb, F.; Kohlhoff, M.; Bogdanoff, P.; Chernev, P.; Zaharieva, I.; Dau, H. *Energy Environ. Sci.* **2015**, *8*, 661−674.
(85) Bergmann, A.; Martinez-Moreno, E.; Teschner, D.; Chernev, P.; Gliech, M.; de Araújo, J. F.; Reier, T.; Dau, H.; Strasser, P. *Nat. Commun.* **2015**, *6*, 8625.
(86) de Groot, F. *Chem. Rev.* **2001**, *101*, 1779−1808.
(87) de Groot, F. M. F. *J. Electron Spectrosc. Relat. Phenom.* **1994**, *67*, 529−622.
(88) Frazer, B. H.; Gilbert, B.; Sonderegger, B. R.; De Stasio, G. *Surf. Sci.* **2003**, *537*, 161−167.
(89) Smythe, D. J.; Brenan, J. M.; Bennett, N. R.; Regier, T.; Henderson, G. S. *J. Non-Cryst. Solids* **2013**, *378*, 258−264.
(90) Kundu, S.; Ciston, J.; Senanayake, S. D.; Arena, D. A.; Fujita, E.; Stacchiola, D.; Barrio, L.; Navarro, R. M.; Fierro, J. L. G.; Rodriguez, J. A. *J. Phys. Chem. C* **2012**, *116*, 14062−14070.
(91) Wang, H.; Ge, P.; Riordan, C. G.; Brooker, S.; Woomer, C. G.; Collins, T.; Melendres, C. A.; Graudejus, O.; Bartlett, N.; Cramer, S. P. *J. Phys. Chem. B* **1998**, *102*, 8343−8346.
(92) Bora, D. K.; Cheng, X.; Kapilashrami, M.; Glans, P. A.; Luo, Y.; Guo, J.-H. *J. Synchrotron Radiat.* **2015**, *22*, 1450−1458.
(93) Klaus, S.; Louie, M. W.; Trotochaud, L.; Bell, A. T. *J. Phys. Chem. C* **2015**, *119*, 18303−18316.
(94) McIntyre, N. S.; Zetaruk, D. G. *Anal. Chem.* **1977**, *49*, 1521−1529.
(95) Ali-Loytty, H.; Louie, M. W.; Singh, M. R.; Li, L.; Sanchez Casalongue, H. G.; Ogasawara, H.; Crumlin, E. J.; Liu, Z.; Bell, A. T.; Nilsson, A.; Friebel, D. *J. Phys. Chem. C* **2016**, *120*, 2247−2253.
(96) Ahmed, F.; Kumar, S.; Arshi, N.; Anwar, M. S.; Heun Koo, B. *CrystEngComm* **2012**, *14*, 4016−4026.
(97) Chan, C. S.; De Stasio, G.; Welch, S. A.; Girasole, M.; Frazer, B. H.; Nesterova, M. V.; Fakra, S.; Banfield, J. F. *Science* **2004**, *303*, 1656−1658.
(98) Nishizawa, K.; Kurahashi, N.; Sekiguchi, K.; Mizuno, T.; Ogi, Y.; Horio, T.; Oura, M.; Kosugi, N.; Suzuki, T. *Phys. Chem. Chem. Phys.* **2011**, *13*, 413−417.
(99) Seidel, R.; Thurmer, S.; Winter, B. *J. Phys. Chem. Lett.* **2011**, *2*, 633−641.
(100) Langell, M. A.; Anderson, M. D.; Carson, G. A.; Peng, L.; Smith, S. *Phys. Rev. B: Condens. Matter Mater. Phys.* **1999**, *59*, 4791−4798.